Ceramics International xxx (xxxx) xxx

Contents lists available at ScienceDirect

Ceramics International

journal homepage: www.elsevier.com/locate/ceramint

Anisotropic mechanical enhancements of additively manufactured silica with boron nitride nanotubes

Dingli Wang [a], Zihan Liu [a], Nasim Anjum [a], Yingchun Jiang [a], Changhong Ke [a,b,*]

[a] Department of Mechanical Engineering, State University of New York at Binghamton, Binghamton, NY, 13902, USA
[b] Materials Science and Engineering Program, State University of New York at Binghamton, Binghamton, NY, 13902, USA

ARTICLE INFO

Keywords:
Boron nitride nanotubes
Ceramics
Additive manufacturing
Mechanical enhancement
Microstructures

ABSTRACT

Additive manufacturing (AM) is transforming the manufacturing and applicability of ceramic materials. However, AM-produced ceramics typically exhibit anisotropic and inferior mechanical properties as compared to conventionally manufactured counterparts because of inherent cracks and defects, which substantially impair their potential applications. In this study, we investigate the reinforcement of AM ceramics with boron nitride nanotubes (BNNTs). Incorporating small amounts of BNNTs (up to 0.4 wt%) into silica structures fabricated by digital light processing techniques yields remarkable property enhancements, measured both in-plane and along the thickness (build) directions. Specifically, flexural strength increases by up to 140 %, and fracture toughness increases by up to 150 %. Furthermore, incorporating BNNTs increases the anisotropy ratio (in-plane vs. through-thickness direction) to 1.6 from 1.24 for flexural strength and to 0.96 from 0.61 for fracture toughness. Mechanical failure in BNNT-reinforced silica predominantly occurs within the matrix and is characterized by an effective interfacial shear stress of 136 MPa. *In situ* scanning electron microscopy single nanotube pullout measurements reveal an exceptionally high interfacial shear strength, confirming strong interfacial interactions in the AM BNNT-silica. Microstructural analyses indicate that incorporating BNNTs reduces crystallite size and lattice strain while simultaneously promoting phase transformation. The observed synergistic effects—comprising efficient load transfer from the silica matrix to BNNTs and advantageous microstructural alterations induced by BNNT incorporation—significantly enhance the mechanical performance of silica nanocomposites. This research offers critical insights into the reinforcement mechanisms of BNNTs within AM ceramics, contributing to the optimal design and manufacturing of lightweight, robust, and durable ceramic materials.

1. Introduction

Ceramics are extensively used in aerospace applications, including engine components and thermal protection systems, because of their lightweight and high-strength properties, low thermal expansion, excellent dielectric performance, and outstanding chemical resistance [1–3]. Conventional molding and machining methods are often insufficient for fabricating ceramic components with demanding geometries or multifunctional complexity, because of their intrinsic brittleness. Additive manufacturing (AM) is revolutionizing the manufacturing and applications of ceramic materials, offering high precision, improved efficiency, design flexibility, and effective use of raw materials [4]. Ceramics produced through vat photopolymerization (VPP)-based AM techniques, commonly referred to as stereolithography apparatus (SLA) or digital light processing (DLP), offer notable advantages, including high precision and excellent surface quality [5–7]. Despite these benefits, AM ceramics typically exhibit anisotropic and mechanically inferior properties as compared to conventionally manufactured counterparts, primarily because of the presence of inherent cracks and defects. These shortcomings significantly limit their functional performance and practical applications. For instance, the flexural strength of monolithic silica fabricated using SLA/DLP methods often remains below 15 MPa [8–10], which is markedly lower than the values exceeding 50 MPa achieved via traditional molding techniques [11]. The most critical challenge lies in the formation of structural defects, such as cracks, pores, and delamination, during the high-temperature debinding and sintering stages, which severely impede the industrial adoption of AM ceramics [12,13].

Reinforcing AM ceramics with nanofillers presents a promising strategy to overcome their mechanical limitations. Boron nitride

* Corresponding author. Department of Mechanical Engineering, State University of New York at Binghamton, Binghamton, NY, 13902, USA.
E-mail address: cke@binghamton.edu (C. Ke).

https://doi.org/10.1016/j.ceramint.2025.11.251
Received 14 July 2025; Received in revised form 3 November 2025; Accepted 18 November 2025
Available online 19 November 2025

nanotubes (BNNTs) are among the most promising nanofillers for ceramic matrices because of their low density, large surface-to-volume ratios, and outstanding physical properties and chemical stability. BNNTs are among the strongest known materials, with a Young's modulus reaching up to 1.3 TPa and a tensile strength of up to 60 GPa [14–16]. They demonstrate excellent thermal stability, retaining their crystalline structure up to 900 °C in air [17] and over 1800 °C in inert atmospheres [18]. The transverse flexibility of BNNTs [19,20] enables them to conform closely to ceramic grain surfaces, promoting intimate interfacial contact that is advantageous for efficient load transfer. Furthermore, the partially ionic and covalent nature of B–N bonding contributes to an anisotropic energy landscape at the binding interface with ceramics, enhancing shear resistance and enabling energy dissipation via frictional interfacial sliding during nanotube pullout [21,22]. Incorporation of BNNTs can also induce favorable microstructural modifications in the ceramic matrix, such as increased crystallinity, grain refinement, and reduced lattice strain, thereby improving the bulk mechanical performance [11,23,24]. In combination with their characteristically weak light absorption, these properties make BNNTs exceptionally well-suited for reinforcing ceramics produced via VPP-based AM processes.

BNNTs have been shown to significantly reinforce and toughen ceramic matrices when incorporated through conventional molding processes. For example, the addition of 0.1–0.5 wt% BNNTs into silica enhances flexural strength by 51–153 % and fracture toughness by 54–167 % [23]. Incorporating 5 wt% BNNTs into silica leads to a remarkable 131 % increase in flexural strength and a 109 % improvement in fracture toughness [11]. Similarly, the inclusion of 1.5 wt% BNNTs in alumina yields a 59 % increase in flexural strength and a 17 % enhancement in fracture toughness [25]. A recent study shows that adding 1 wt% of BNNTs into polymer-derived silicon oxycarbide increases flexural strength by 150 % and fracture toughness by 230 % [26]. While BNNTs have demonstrated promising reinforcement effects in conventionally manufactured ceramics, studies on reinforcing AM ceramics with BNNTs remain scarce [24,27].

In this study, we explore the mechanical reinforcement effects of BNNTs in AM silica produced via DLP. Particular emphasis is placed on evaluating the enhancement of bulk mechanical properties and the local interfacial load transfer characteristics. The results demonstrate notable improvements in bulk mechanical performance and anisotropic reinforcement efficiency, which are attributed to effective interfacial load transfer at the BNNT-matrix interface and beneficial microstructural modifications within the ceramic matrix. These findings provide valuable insights into the reinforcement mechanisms of BNNTs in AM ceramics, advancing the design of high-performance ceramic materials with tailored mechanical properties enabled by additive manufacturing.

2. Materials and methods

2.1. Materials

BNNTs used in this study (BNNT Materials, LLC) are synthesized using a high-temperature–pressure (HTP) technique [28], yielding a product with an approximately 88 % BNNT purity and over 99 % hexagonal boron nitride (h-BN) content [23]. HTP-BNNTs are predominantly double-walled, with a median diameter of 2.9 nm [19,29]. Two types of high-purity silica powders (>99 %, US Research Nanomaterials, Inc.) are employed: one with an average particle size of ~1 μm (quartz) and the other with an average size of 400 nm (amorphous), and their X-ray diffraction (XRD) results are shown in Supplementary Fig. S1 of the Supplementary Information. Two types of photosensitive resins are used: 1,6-hexanediol diacrylate (HDDA, Thermo Fisher Scientific Inc.) and polyethylene glycol diacrylate (PEGDA, Sigma-Aldrich Co.). The formulation includes surfactant BYK-111 (BYK Additives and Instruments) and photoinitiator diphenyl (2,4,6-trimethylbenzoyl) phosphine oxide (TPO, Sigma-Aldrich Co.).

2.2. Sample preparation

As-received BNNTs are first dispersed in acetone using ultrasonication (Branson 1510 sonicator) for 1 h to form a homogeneous suspension. A mixture of 1-μm and 400-nm silica powders, at a mass ratio of 4:1, is then added to the BNNT-acetone suspension. Following sonication, the BNNT-silica suspension is dried at 90 °C for 12 h to remove acetone. The dried composite powder is subsequently ground, sieved, and incorporated into a premixed resin solution consisting of HDDA and PEGDA in a volume ratio of 9:1. Surfactant BYK-111 and photoinitiator TPO are added at 1.5 wt% relative to the solid content and 1.0 wt% relative to the liquid content, respectively. The silica content constitutes 55 vol% of the printable slurry. The final mixture is homogenized using a DAC 330-100 L centrifugal mixer (FlackTek Inc.) at 3000 rpm for 1 h.

3D printing of the BNNT-silica slurry is carried out using a DLP printer (Hunter, Flashforge Inc.) with a layer thickness of 50 μm and an exposure time of 3 s per layer. The printed green bodies (Fig. 1a) undergo a three-stage thermal debinding in air, reaching up to 700 °C to remove organic binders. The process involves an initial temperature ramp from room temperature (~25 °C) to 396 °C at a rate of 0.5 °C/min, followed by a 30-min hold; a second ramp to 492 °C at the same rate, with another 30-min hold; and a final ramp to 700 °C at 1 °C/min, held for 1 h before natural cooling to room temperature. The debinding temperatures of 396 °C and 492 °C are selected based on thermogravimetric analysis (TGA) and the corresponding derivative thermogravimetric (DTG) profile (Supplementary Fig. S2), aiming to minimize crack formation during decomposition. The nanocomposite specimens are sintered in an argon atmosphere inside a pressureless furnace (STV-1600C, Sentro Tech, Inc.) at 1400 °C with a heating rate of 2 °C/min and a dwell time of 1 h. After sintering, the samples are cooled to 800 °C at a rate of 2 °C/min, followed by natural cooling to room temperature. Silica nanocomposites with BNNT loadings of up to 0.4 wt% are successfully fabricated. Unless otherwise stated, all BNNT concentrations reported in this study are expressed as weight percent.

2.3. Characterization

The viscosities of BNNT/silica slurries are measured using a rotational rheometer (Discovery HR30, TA Instruments). The weight loss behavior of BNNT-silica green bodies is evaluated in air using a thermogravimetric analyzer (TGA, Q50, TA Instruments), with heating from ambient temperature to 800 °C at a rate of 10 °C/min. The bulk density of the specimen is determined using Archimedes' method with deionized water as the immersion medium, expressed as $\rho_c = m_1\rho_w/(m_0 - m_2)$, where $\rho_w = 1000$ kg/m^3 is the density of water, and m_0, m_1, and m_2 correspond to the dry, wet, and suspended weights of the specimen, respectively [30]. Quasi-static three-point bending and single-edge notched beam (SENB) fracture toughness tests are performed using a micromechanical tester (ADMET) at a displacement rate of 50 μm/min. A micro-computed tomography (micro-CT) system (Nanome|X, Baker Hughes-GE) is employed to assess internal defects and porosity. Microstructural and morphological characterization is carried out using a field-emission scanning electron microscope (SEM, Supra 55, Zeiss). Raman spectroscopy is performed with a Renishaw InVia Raman microscope, equipped with a 532 nm excitation laser, a 50 × objective lens, and a laser spot size of approximately 1.2 μm. *In situ* Raman micromechanical measurements are conducted using a micromechanical tester (TST350, Linkam Scientific Instruments) integrated with the Renishaw Raman system. XRD analysis is conducted using a PANalytical X'Pert PRO diffractometer, equipped with a sealed Cu tube for Cu Kα radiation (~1.54 Å), operating at 45 kV and 40 mA.

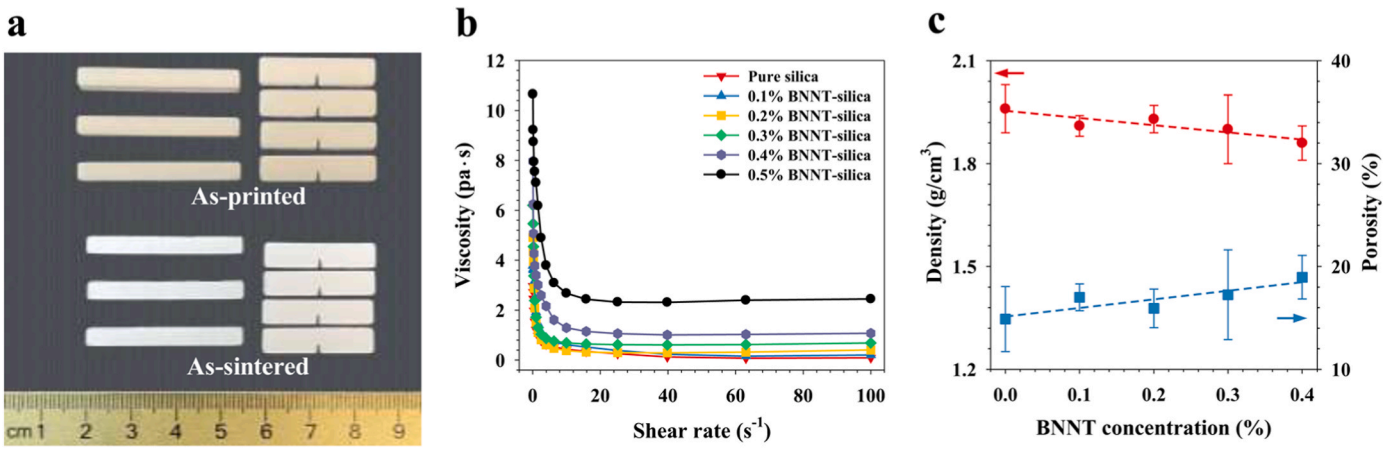

Fig. 1. Manufacturing and structural characterization of BNNT-silica nanocomposites: (a) Optical images of green parts and sintered parts; (b) Viscosity of silica slurries; (c) Density and porosity. (For interpretation of the references to colour in this figure legend, the reader is referred to the Web version of this article.)

3. Results and discussion

3.1. Rheological and structural properties

A critical step in the fabrication of ceramic components via DLP involves preparing a photo-curable slurry with suitable rheological properties [31]. As shown in Fig. 1b, viscosity measurements indicate that BNNT/silica slurries exhibit shear-thinning behavior as the shear rate increases, consistent with the characteristics of a non-Newtonian pseudoplastic fluid [32]. The viscosity initially decreases and then levels off as the shear rate continues to increase. The rheological behavior of the ceramic slurry is described using the power-law model [33], given as

$$\eta = K\dot{\gamma}^{n-1}, \quad (1)$$

where η represents the viscosity, $\dot{\gamma}$ is the shear rate, n is the power-law index, and K is the flow consistency index, which reflects the overall viscosity of the slurry. Notably, the K value for BNNT/silica slurries increases significantly from 1.23 to 6.11 as the BNNT concentration rises from 0 % to 0.5 % (Table 1), an effect attributed to the high aspect ratio of BNNTs. In DLP printing, the effective layer-by-layer replenishment of the slurry before UV curing requires a viscosity below 2 Pa·s at a shear rate of 10 s^{-1} [34]. However, the slurry containing 0.5 % BNNT exceeds this viscosity threshold under those conditions. Consequently, the maximum BNNT loading in this study is limited to 0.4 %.

Fig. 1c presents the variations in density and porosity of BNNT-silica. As BNNT content increases, a decreasing trend in density is observed, accompanied by a corresponding increase in porosity. These observations are consistent with previous studies on BNNT-reinforced ceramics [35,36]. During pressureless sintering, densification is primarily driven by the reduction of surface energy, which facilitates atomic diffusion and the development of sintering necks between neighboring silica particles. In contrast, the poor interfacial wettability between BNNTs and silica, relative to that among silica particles, causes BNNTs to accumulate along particle boundaries. The segregation disrupts direct particle-to-particle contact and hinders neck formation, thereby impeding local mass transport and ultimately limiting the densification of the silica matrix.

Cure depth is a key parameter for balancing interlayer adhesion and dimensional accuracy in DLP printing: insufficient cure depth weakens interlayer bonding, whereas excessive cure depth degrades dimension precision. In this study, the single-layer thickness is set to 50 μm, and the exposure time is fixed at 3 s across all BNNT loadings to preserve a one-factor (BNNT concentration) experimental design. For BNNT concentrations from 0 to 0.4 %, the measured cure depths using optical microscopy are 228 ± 21 μm (0 %), 224 ± 17 μm (0.1 %), 214 ± 19 μm (0.2 %), 207 ± 15 μm (0.3 %), and 196 ± 21 μm (0.4 %). All of those values fall within the commonly recommended range of 3–5 times the layer thickness (i.e., 150–250 μm) [37].

Table 1
The fitted power-law model parameters of BNNT-silica slurry and the corresponding R-squared (R^2) value.

Materials	K	n	R^2
Pure silica	1.23	0.58	0.98
0.1% BNNT-silica	1.82	0.62	0.95
0.2% BNNT-silica	1.65	0.49	0.98
0.3% BNNT-silica	2.05	0.50	0.98
0.4% BNNT-silica	3.33	0.65	0.99
0.5% BNNT-silica	6.11	0.75	0.96

3.2. Bulk mechanical properties

The mechanical properties of DLP-fabricated ceramics are inherently anisotropic because of weak interlayer bonding [9]. To investigate the anisotropic reinforcement effects of BNNTs, we performed three-point bending and fracture toughness tests along two orthogonal orientations, as illustrated in Fig. 2a and b. In orientation A, the loading force is applied parallel to the in-plane direction of the ceramic layers (i.e., perpendicular to the build direction). In contrast, in orientation B, the loading force is applied along the build (i.e., through-thickness) direction. While both orientations involve deformation of the printed ceramic layers, interlayer shear deformation occurs only in orientation B. Consequently, the DLP-printed composite specimens exhibit higher mechanical strength in orientation A.

Representative flexural stress-strain curves for BNNT-silica in orientations A and B are shown in Fig. 2c and d, respectively (see Supplementary Information for measurement procedures and analysis details). Fig. 2e compares the measured flexural strength and fracture toughness for both testing orientations, with the data summarized in Table 2. The flexural strength of pure silica in orientation A (~14.0 MPa) is approximately 2.7 MPa higher than in orientation B (~11.3 MPa), which can be attributed to interlayer shear deformations during bending in orientation B [38]. This observation aligns with prior findings that interlayer strength is lower than in-plane strength in DLP-fabricated ceramics [39].

For both testing orientations, the flexural strength increases with BNNT concentration. Specifically, the incorporation of 0.4 % BNNTs results in a 140 % increase in flexural strength to ~33.6 MPa in orientation A, compared to an 86 % increase to ~21.0 MPa in orientation B. These results confirm the reinforcing effect of BNNTs in DLP-printed silica, with a more pronounced improvement observed in orientation

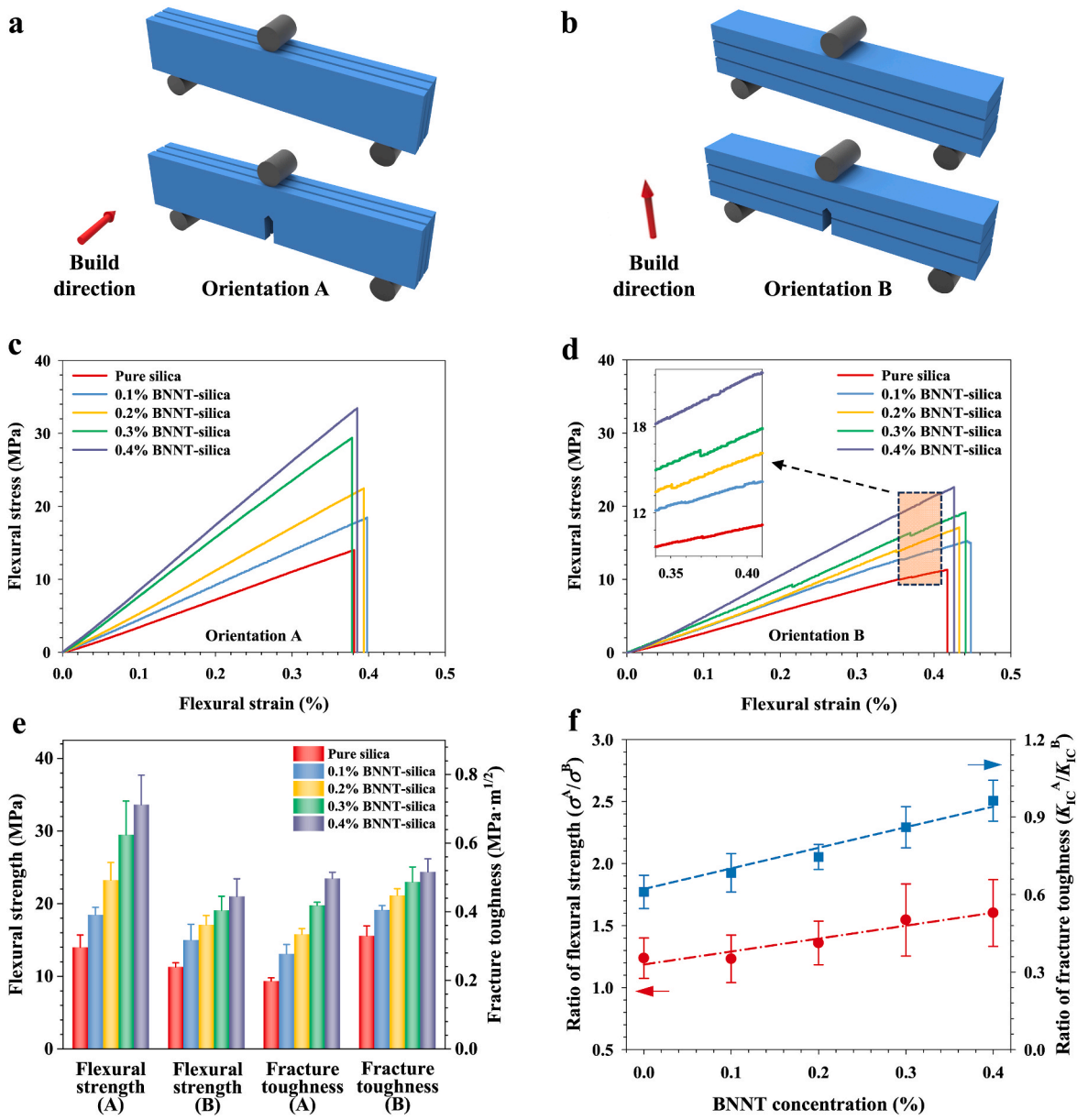

Fig. 2. Bulk mechanical characterization of BNNT-silica nanocomposites: Schematic representation of three-point bending test and fracture toughness evaluation for (a) testing orientation A and (b) testing orientation B; Typical flexural stress-strain curves for (c) testing orientation A and (d) testing orientation B; (e) Flexural strength and fracture toughness; (f) Anisotropic ratios of flexural strength and fracture toughness.

Table 2
Mechanical and density properties of DLP-manufactured BNNT-silica nanocomposites.

BNNT loading (%)	Flexural strength (MPa)		Fracture toughness (MPa·m$^{1/2}$)		Failure strain (‰)		Density (g/cm^3)
	Orientation A	Orientation B	Orientation A	Orientation B	Orientation A	Orientation B	
0	14.0 ± 1.7	11.3 ± 0.6	0.20 ± 0.01	0.33 ± 0.03	3.9 ± 0.5	4.2 ± 0.3	1.96 ± 0.07
0.1	18.5 ± 1.1	15.0 ± 2.2	0.28 ± 0.03	0.41 ± 0.01	4.0 ± 0.6	4.5 ± 0.4	1.91 ± 0.02
0.2	23.2 ± 0.5	17.1 ± 1.3	0.33 ± 0.02	0.45 ± 0.02	3.9 ± 0.4	4.3 ± 0.3	1.93 ± 0.04
0.3	29.5 ± 4.7	19.1 ± 1.9	0.42 ± 0.01	0.49 ± 0.04	3.8 ± 0.4	4.4 ± 0.4	1.90 ± 0.10
0.4	33.6 ± 4.1	21.0 ± 2.4	0.50 ± 0.02	0.52 ± 0.04	3.9 ± 0.5	4.2 ± 0.3	1.86 ± 0.05

A. This suggests that interlayer defects in DLP-fabricated ceramics reduce the overall strength in orientation B and limit the effectiveness of BNNTs in enhancing mechanical performance.

In contrast to flexural strength, the fracture toughness (K_{IC}) of DLP-fabricated silica exhibits an opposite trend. The K_{IC} of pure silica in orientation A (~0.20 MPa·m$^{1/2}$) is significantly lower than that in orientation B (~0.33 MPa·m$^{1/2}$). The difference is attributed to the crack-deflection mechanism induced by interlayer cracks in orientation B, as illustrated in Fig. 3. In orientation A, once the crack tip initiates, it propagates rapidly through the material, leading to catastrophic failure without noticeable crack deflection, owing to the intrinsic brittleness of the ceramic matrix. In contrast, in orientation B, after the initial layer

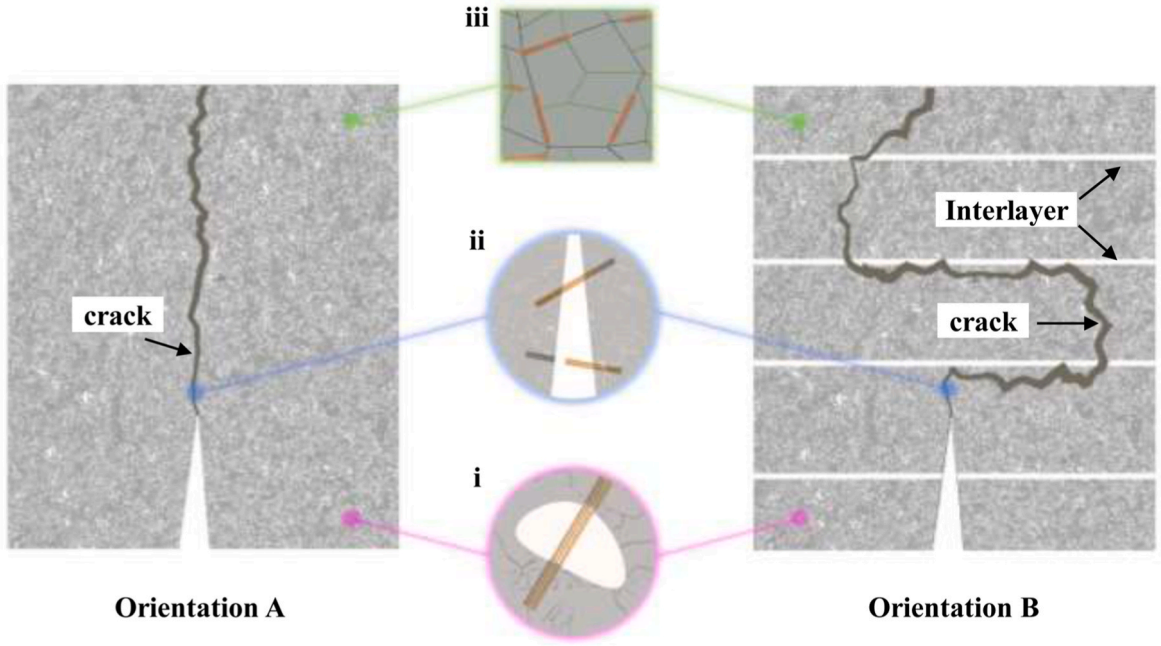

Fig. 3. Schematic illustration of the reinforcement mechanisms in DLP 3D-printed BNNT-silica nanocomposites in two testing orientations: (i) pore stiffening; (ii) nanotube pullout and crack bridging; (iii) grain refinement. The drawings are not to scale.

cracks and fractures, the interlayer cracks, oriented perpendicular to the loading direction, act as barriers to direct crack propagation. These interfaces promote crack deflection [40], forcing the crack to deviate from its original path rather than advancing straight into the adjacent layer. This deflection process increases the fracture surface area, dissipates mechanical energy, and thereby enhances the material's fracture resistance and toughness.

The addition of BNNTs consistently enhances fracture toughness in both testing orientations while reducing the disparity between them. Incorporating 0.4 % BNNTs increases the K_{IC} by 150 % to ~0.50 MPa·m$^{1/2}$ in orientation A, and by 58 % to about 0.52 MPa·m$^{1/2}$ in orientation B. The results suggest that although interlayer defects can help impede crack propagation, they diminish the effectiveness of BNNTs in improving fracture toughness.

Overall, the incorporation of 0.4 % BNNTs increases the anisotropy ratio (in-plane vs. through-thickness direction) from 1.24 to 1.6 for flexural strength and from 0.61 to 0.96 for fracture toughness, as shown in Fig. 2f.

The failure strain of BNNT-silica in orientation A ranges from 0.38 to 0.40 %, which is notably lower than the failure strain of 0.42–0.45 % observed in orientation B. This difference is attributed to the aforementioned crack deflection mechanisms active in orientation B, which enhance the composite's deformability. Supporting this interpretation, the stress–strain curves for orientation B exhibit more abrupt downward discontinuities (see zoomed-in plot in Fig. 2d), indicative of progressive fracture events caused by crack twisting and meandering due to interlayer defects (Fig. 3). This tortuous crack path facilitates localized energy dissipation and plastic deformation, thereby enhancing the material's ductility.

Fig. 4 compares the measured flexural strength from this study with literature values for 3D-printed silica and silica-based composites, which are summarized in supplementary Table S1. Reported flexural strength values for pure silica range from 11.4 to 13.3 MPa, which aligns closely with our measured average value of ~12.7 MPa. The results demonstrate that our processing and sintering conditions successfully produce well-densified silica with reliable mechanical properties. For silica composites containing various fillers, literature values range from 12.1 to 24.3 MPa. In comparison, the flexural strength of 0.4 % BNNT-silica

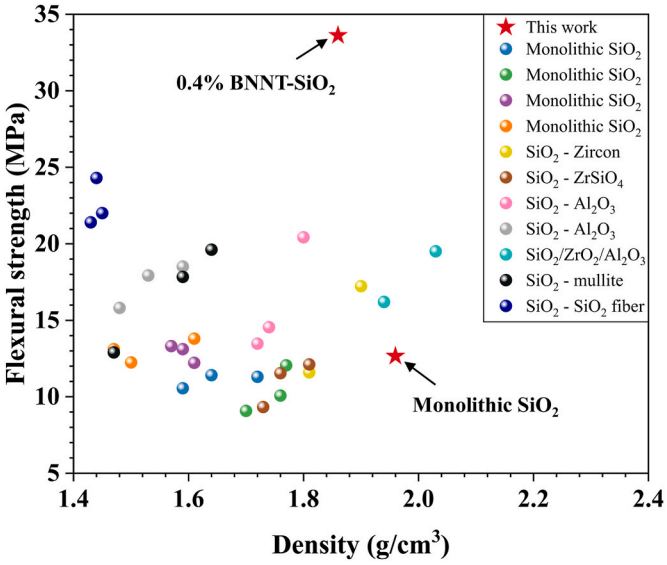

Fig. 4. Comparison of the flexural strength obtained in this work with the literature values for silica and silica composites manufactured via SLA/DLP techniques, which are listed in supplementary Table S1 with reference sources.

(33.6 MPa) surpasses the reported values by 38–178 %, while retaining the inherent low-density characteristics of silica. The result further highlights the exceptional reinforcing capability of BNNTs in ceramic matrices, even at low loadings.

3.3. Structural defects and failure modes

Micro-CT analysis of BNNT-silica, as shown in Fig. 5a, reveals uniformly distributed micron-sized pores within the specimen, consistent with previously reported high porosity in DLP-fabricated silica [8,9]. Larger defects exceeding 100 μm are observed and are primarily attributed to delamination, with cracks predominantly oriented perpendicular to the build direction. Further examination by SEM, as

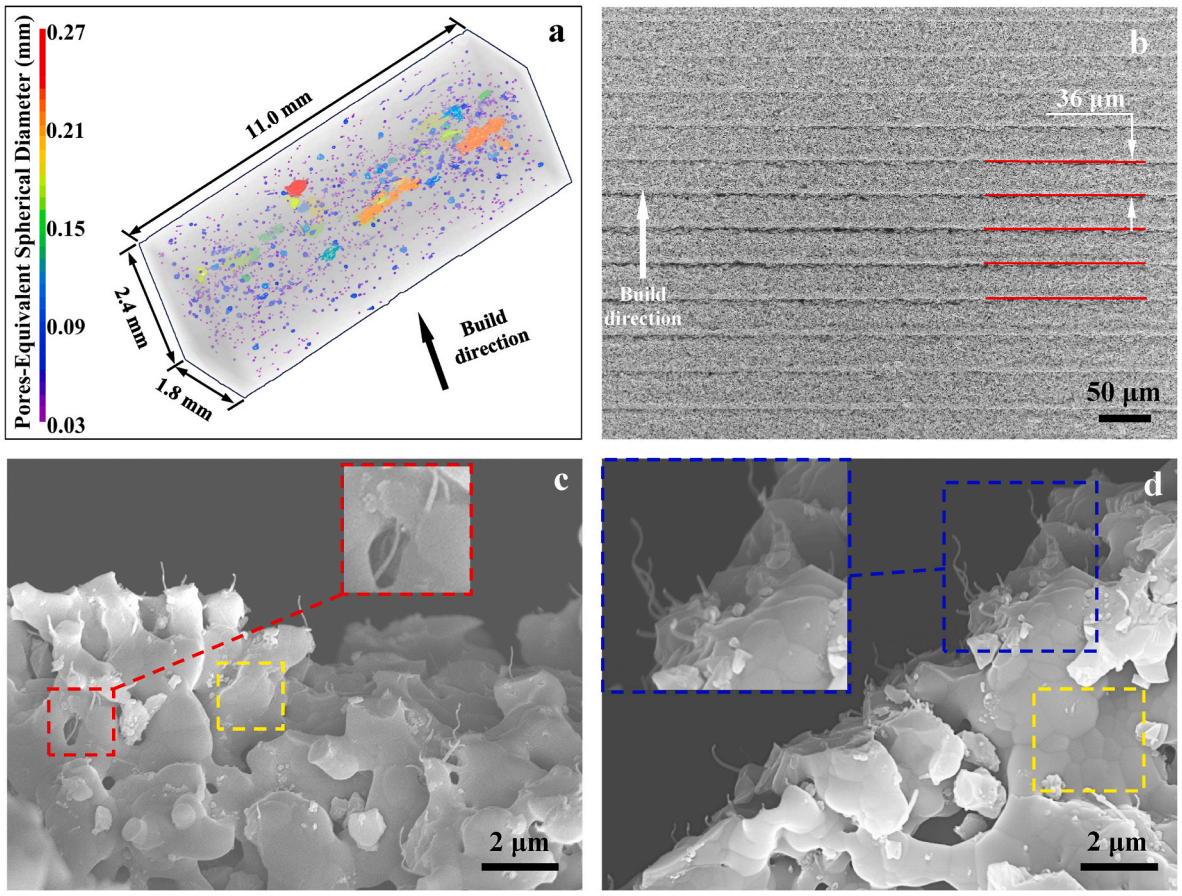

Fig. 5. Internal defects and failure modes of BNNT-silica nanocomposites: (a) Micro-CT analysis of the spatial and size distributions of defects; (b) SEM image showing the interlayer defects; (c, d) SEM images of fracture surfaces of 0.4 % BNNT-silica. The yellow dashed boxes highlight sintering necks. The red dashed boxes highlight a nanotube spanning across a pore. The blue dashed boxes highlight protruding nanotubes from the matrix. (For interpretation of the references to colour in this figure legend, the reader is referred to the Web version of this article.)

displayed in Fig. 5b, reveals that these delamination and interlayer defects primarily arise from separation and shrinkage forces during the green body formation stage, which exceed the bonding strength of the binder [13]. These interlayer defects reduce the composite's mechanical strength.

SEM images of a fractured 0.4 % BNNT-silica specimen, as shown in Fig. 5c and d, reveal that BNNTs are predominantly observed as discrete, well-separated nanotubes rather than clustered agglomerates, indicating uniform dispersion throughout the silica matrix. Well-developed sintering necks between silica particles, highlighted by yellow dashed boxes, demonstrate effective densification. Additionally, nanoscale pores resulting from binder removal during thermal debinding [13] are evident. These pores act as stress concentrators [41], amplifying local stresses and promoting crack initiation, which compromises the bulk mechanical performance.

Nanotube bridging across these pores, as indicated by the red zoom-in box in Fig. 5c, helps mitigate the adverse effects of porosity. Because of their high aspect ratios and strong binding interactions with the matrix, BNNTs can span across developing cracks, facilitate load transfer across crack faces, and shield crack tips from applied stresses. Furthermore, protruding nanotubes, highlighted by the blue zoom-in box in Fig. 5d, contribute to energy dissipation through mechanisms such as fracture, interfacial debonding, and frictional sliding during pullout, thereby enhancing the composite's toughness. The nanotube pullout and crack bridging, and pore stiffening, as illustrated in Fig. 3, are two of the key reinforcing mechanisms in BNNT-ceramic nanocomposites.

3.4. Characterization of local stress transfer

3.4.1. In situ Raman microscopy measurements

Fig. 6a shows representative Raman spectra of monolithic silica, pure BNNTs, and 0.4 % BNNT-silica. Both BNNTs and BNNT-silica exhibit a distinct G-band at ~1369 cm^{-1} [42]. Raman peaks near 1074 cm^{-1} and 1160 cm^{-1} correspond to cristobalite and quartz, respectively. Fig. 6b presents a typical Raman map over a 60 × 48 μm^2 area, using a step size of 1.2 µm. The presence of the BNNT Raman signal throughout the mapped area confirms a uniform dispersion of nanotubes within the silica matrix, in agreement with SEM observations. Furthermore, polarized Raman microscopy measurements shown in Supplementary Fig. S3 reveal that the embedded BNNTs exhibit a random orientation within the matrix. Therefore, the anisotropic mechanical properties of BNNT-silica can be attributed solely to the layering effects of 3D printing, rather than the orientation of BNNTs.

Fig. 7a illustrates *in situ* Raman microscopy measurements of local mechanical deformations in BNNT-silica. Rectangular nanocomposite bars of 36 × 4 × 3 mm (length × width × thickness) are subjected to three-point bending, with the build direction aligned along the width axis (z-axis in Fig. 7a). The bending behavior of the composite is assumed to follow classical beam theory, approximating isotropic deformation, which is confirmed by measurements using digital image correlation (DIC) techniques [23] (see Supplementary Fig. S4 for details). Raman spectra are recorded at three specific points: A, B, and C. Point A, located at the tensile surface, experiences the maximum matrix strain; Point C lies near the neutral axis, where strain is minimal or negligible; Point B, situated halfway between A and C, undergoes

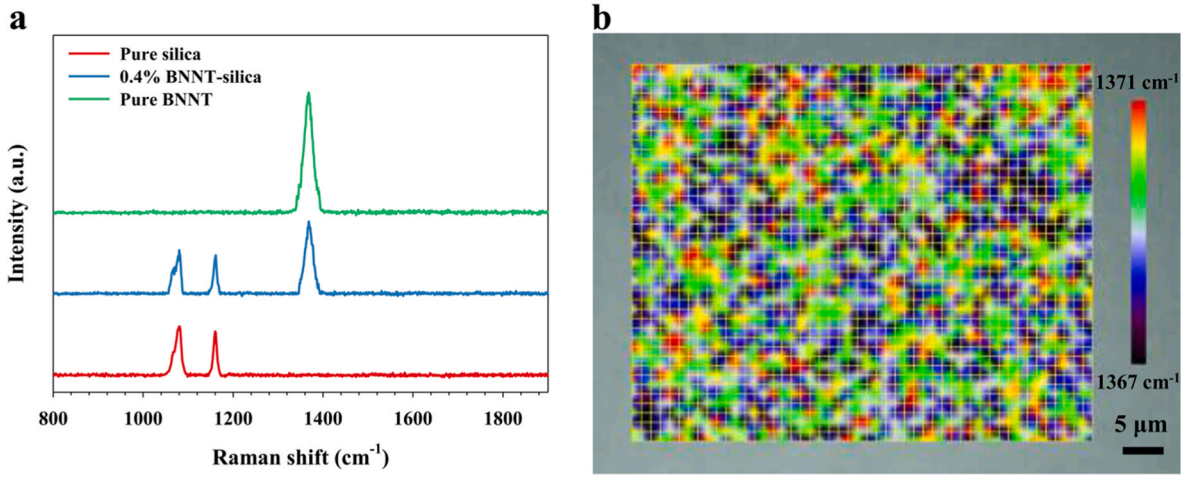

Fig. 6. Raman characterization: (a) Raman spectra of pure silica, 0.4 % BNNT-silica, and pure BNNT; (b) Typical Raman area map of the G-band peak frequency of BNNTs in 0.4 % BNNT-silica with a step size of 1.2 μm.

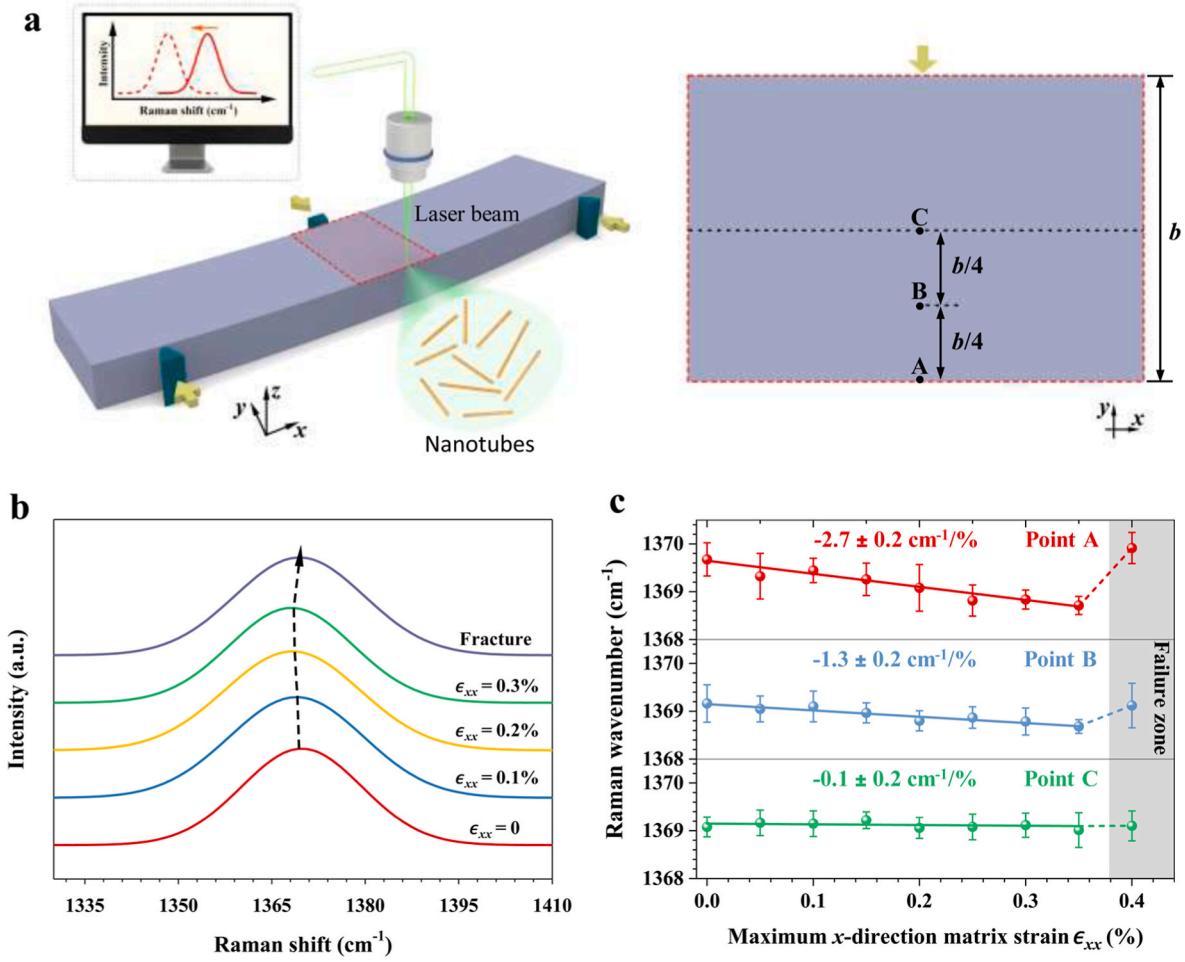

Fig. 7. In situ Raman micromechanical characterization of BNNT-silica nanocomposites (0.4 %): (a) Schematic illustration of in situ three-point bending Raman testing (the build direction along the z-axis): 3D configuration (left) and in-plane positions of points A, B and C (right); (b) Representative in situ Raman spectra at point A; (c) In situ BNNT Raman peak shifts at points A, B and C correlating with the maximum *x*-direction matrix strain.

approximately half the strain at Point A.

The indenter advances in displacement increments of 25 μm, corresponding to an approximate 0.05 % increase in the maximum matrix tensile strain. Notably, because of the inherently weak resonant Raman scattering in BNNTs, *in situ* Raman measurements in this study are limited to specimens with 0.4 % BNNT content, which exhibit sufficiently strong Raman signals for reliable analysis.

Fig. 7b illustrates the evolution of the Raman G-band at point A under varying matrix strains. A progressive downshift in the G-band peak frequency is observed with increasing strain, indicating B–N bond

elongation and confirming effective interfacial load transfer between nanotubes and the surrounding matrix. Upon specimen failure, the G-band peak frequency returns to its unloaded state, indicating the complete release of mechanical strain within the nanotubes.

Fig. 7c presents the G-band Raman shift as a function of the maximum longitudinal strain (ϵ_{xx}) at the three selected points (A, B, and C). At points A and B, the G-band peak frequency decreases linearly with increasing strain, with slopes of approximately -2.7 cm^{-1}/% and -1.3 cm^{-1}/%, respectively. In contrast, the Raman shift at point C remains nearly unchanged, consistent with its location near the neutral axis. These results confirm effective load transfer from the matrix to BNNTs and demonstrate that failure is dominated by matrix rupture rather than interfacial debonding [43]. The observed effective load transfer is attributed to the uniform dispersion of BNNTs within the silica matrix and strong interfacial bonding [22]. This mechanism is a key contributor to the reinforcement of BNNT-ceramic composites.

3.4.2. Local interfacial load transfer characteristics

The top-left schematic in Fig. 8a shows a random distribution of BNNTs within a matrix, while the bottom-left image presents an equivalent model in which individual BNNTs are embedded uniformly in the matrix at an alignment angle φ relative to the longitudinal direction. In a composite system containing fully randomly oriented nanotubes, the average nanotube strain is equivalent to that of nanotubes oriented at $\varphi = 45^{\circ}$, and is expressed as $\epsilon_{nt}^{ave} = \frac{1-\nu_m}{2}\epsilon_m$ [23], where ϵ_m is the matrix strain and ν_m is the Poisson's ratio of the matrix. The critical failure strain ϵ_{nt}^{ave} is estimated to be ~0.17 % for 0.4 % BNNT-silica, assuming $\nu_m = 0.17$ [44].

The interfacial shear stress (IFSS) within the nanotube-reinforced ceramic nanocomposite is analyzed using the shear-lag micromechanics model [21,22]. The right schematic in Fig. 8a illustrates the simplified single-nanotube nanocomposite configuration, where a nanotube with a diameter D_{nt} is concentrically embedded inside a cylindrical matrix of diameter D_m with the same length l. The pointwise IFSS distribution along the BNNT-silica interface, τ, is expressed as [45]:

$$\tau = \frac{E_{nt}\cdot\epsilon_{nt}^{ave}\cdot p\cdot\cosh(2px/D_{nt})}{2\sinh(pl/D_{nt})}, \tag{2}$$

where x is the coordinate along the longitudinal axis of the nanotube and $p = \sqrt{\frac{E_m}{E_{nt}(1+\nu_m)\log(D_m/D_{nt})}}$, in which E_m and E_{nt} are the Young's moduli of the matrix and nanotubes, respectively. Fig. 8b shows the pointwise distribution of the IFSS at failure strain. The maximum IFSS occurs at the two ends of the nanotube (i.e., $x = \pm l/2$) and is calculated to be ~136 MPa. The corresponding maximum normal stress in the nanotube is calculated to be ~1.8 GPa. The values are obtained using the following parameters: $E_{nt} = 1070$ GPa [46]; $E_m = 70$ GPa [47]; $D_{nt} = 2.9$ nm; D_m is estimated to be ~35.1 nm, calculated based on the densities of silica (2.3 g/cm^3) [48] and BNNTs (1.35 g/cm^3) [43]. Furthermore, a nanotube length $l = 400$ nm is adopted, as the maximum IFSS is found to be

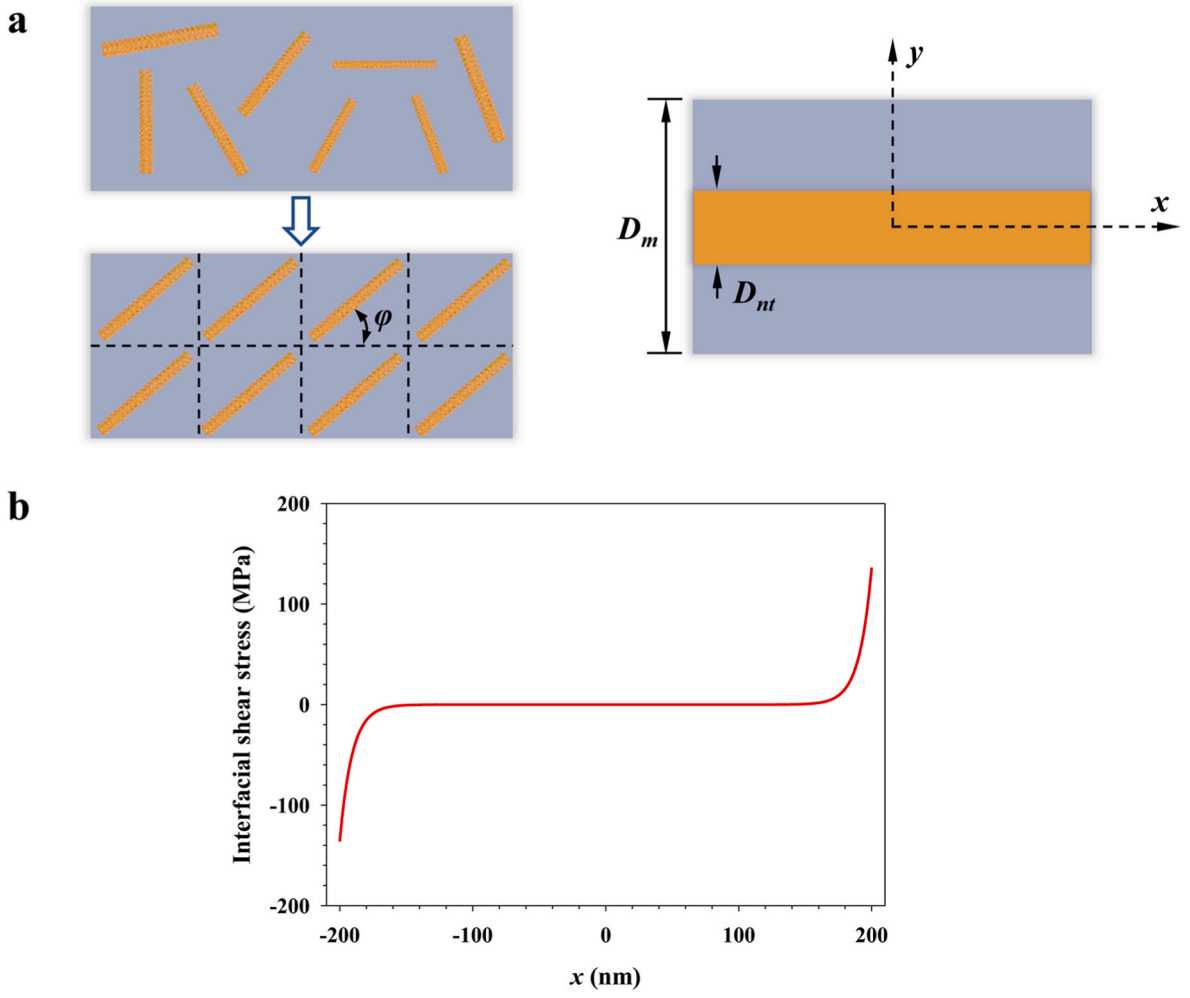

Fig. 8. Interfacial load transfer characteristics inside BNNT-silica nanocomposites: (a) Schematics of a silica composite reinforced with randomly oriented nanotubes (top-left) and equivalent configuration with all nanotubes in the same alignment angle φ (bottom-left), alongside schematic of single nanotube nanocomposite (right); (b) Theoretical predictions of the IFSS distribution along the embedded 400 nm-long BNNT in 0.4 % BNNT-silica at failure strain.

independent of l for $l > 76$ nm based on a threshold stress value of 0.1 MPa.

3.4.3. *In situ* SEM single-nanotube pullout measurements

In situ Raman mechanical testing reveals a purely elastic interfacial behavior between BNNTs and the silica matrix. However, the ultimate interfacial shear strength of the DLP-fabricated BNNT-silica remains to be fully characterized. To address this issue, we employ *in situ* SEM nanomechanical single-nanotube pullout techniques to quantify the interfacial shear strength. The experimental approach has been established in our prior studies on the interfacial strength of nanotube-reinforced polymers [46], metals [47], and ceramics [21]. Briefly, as illustrated in Fig. 9a, a pre-calibrated atomic force microscopy (AFM) cantilever (CSG10, NT-MDT) with a spring constant of 0.14–0.31 N/m is employed as a force sensor. The cantilever is mounted to a 3D piezo-stage capable of moving in all three axes with a spatial resolution of ~1 nm. The AFM tip is maneuvered to contact the free end of a straight, protruding BNNT extracted from a fractured DLP-fabricated BNNT-silica specimen. The longitudinal direction of the selected nanotube aligns with the AFM tip axis. To ensure robust attachment, the free end of the nanotube is welded to the AFM tip via electron beam-induced deposition (EBID) of platinum. An incrementally increasing tensile force is then applied through displacing the AFM probe until the nanotube is either fully extracted from the matrix or fractured. Selected SEM snapshots in Fig. 9b depict a successful single-nanotube pullout event, with a measured pullout force of 262 nN and an embedded nanotube length of 628 nm. The nanotube fracture scenario is exemplified by the SEM snapshots shown in Supplementary Fig. S5.

Three successful single-nanotube pullout measurements are summarized in Table 3, including the one shown in Fig. 9b. The measured pullout force ranges from 262 to 304 nN, with an average value of 289 nN. The corresponding embedded nanotube length ranges from 217 to 698 nm and shows no apparent correlation with the pullout force. The relatively narrow range of the pullout force, despite a much wider variation in the embedded nanotube length, suggests that the pullout force is largely independent of the embedment length—an indication of shear-lag behavior. This observation aligns with the shear-lag analysis presented earlier in Section 3.4.2. Notably, the average pullout force observed here is ~75 % higher than the mean value (~165 nN) previously reported for pulling individual BNNTs from electron-beam-deposited silica, using the same type of nanotubes and the same single-nanotube pullout technique [22]. Unlike the DLP-produced BNNT-silica system investigated here, the BNNT-silica composite film employed in that study was not subjected to thermal treatment.

Table 3
Single-nanotube pullout measurements of BNNT-silica nanocomposites.

Sample number	Pullout force (nN)	Embedded nanotube length (nm)
#1	301	217
#2	262	628
#3	303	698

The strong interfacial bonding observed in the 3D-printed BNNT-silica is likely due to a complex interplay of nanotube straining, local matrix deformation, and enhanced interfacial interactions. One contributing factor is the compressive stress imposed on the BNNTs in both longitudinal and transverse directions during the cooling stage following pyrolysis, driven by the coefficient of thermal expansion (CTE) mismatch between BNNT and silica. This compressive strain promotes intimate contact between nanotubes and the matrix. Additionally, localized transverse deformation of nanotubes may produce a mechanical "lock-in" effect, further increasing the frictional resistance at the interface. A systematic multiscale computational investigation is warranted to further elucidate the underlying mechanisms of BNNT-matrix interfacial interactions.

Nonetheless, the single-nanotube pullout study indicates a strong interface in 3D-printed BNNT-silica. As described by Equation (2), the maximum IFSS at the nanotube entry point scales with the pullout force. The observed ~75 % increase in pullout force translates into a maximum IFSS of approximately 2.2 GPa—extrapolated from the previously reported value (~1.25 GPa) for the binding interface of BNNTs with electron beam-deposited silica [22]. This interfacial shear strength is over one order of magnitude greater than the value (~136 MPa) measured in bulk 3D-printed BNNT-silica using *in situ* Raman techniques. This discrepancy underscores a key insight: the reinforcement potential of BNNTs in ceramic matrices is constrained not by interfacial debonding but by the ceramic matrix's intrinsic mechanical fragility.

3.5. *Microstructures*

The XRD analyses are performed to further study the microstructural influence of BNNTs on the silica matrix. The XRD pattern of BNNT-silica, shown in Fig. 10a, reveals the exclusive presence of cristobalite and quartz phases. The dominant diffraction peaks correspond to cristobalite (101) at approximately 22° and quartz (011) near 26.7°. The absence of a distinct BNNT peak is likely due to the low nanotube concentration and the overlap of the BN (002) diffraction peak with the quartz (011) peak at $2\theta \approx 26.7°$ [11]. Fig. 10b illustrates the variation in the relative peak intensity ratio of cristobalite (101) to quartz (011) as a function of BNNT

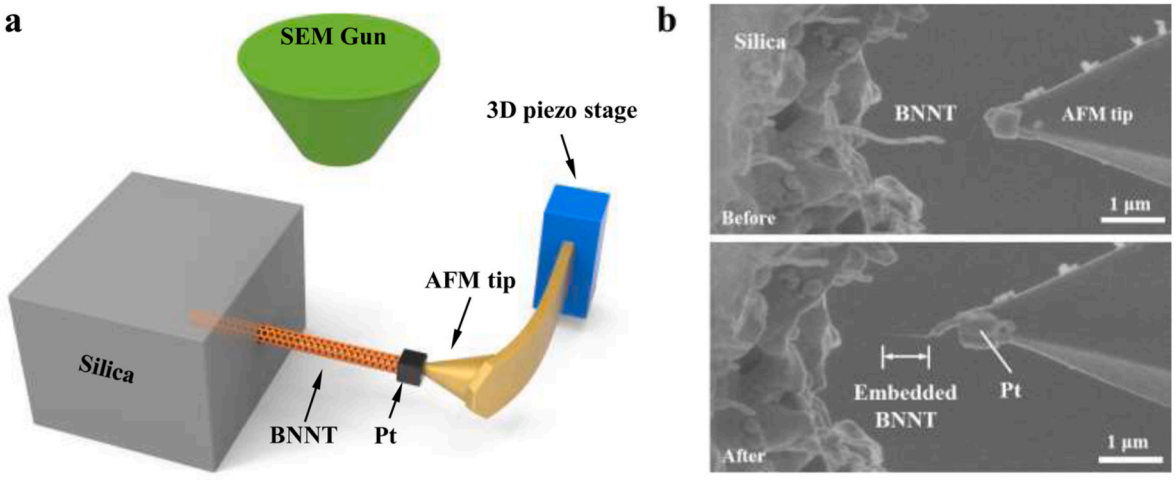

Fig. 9. In situ SEM single-nanotube pullout measurements: (a) Schematic of the setup; (b) Representative SEM images showing the pullout of an individual BNNT from a 3D-printed silica matrix.

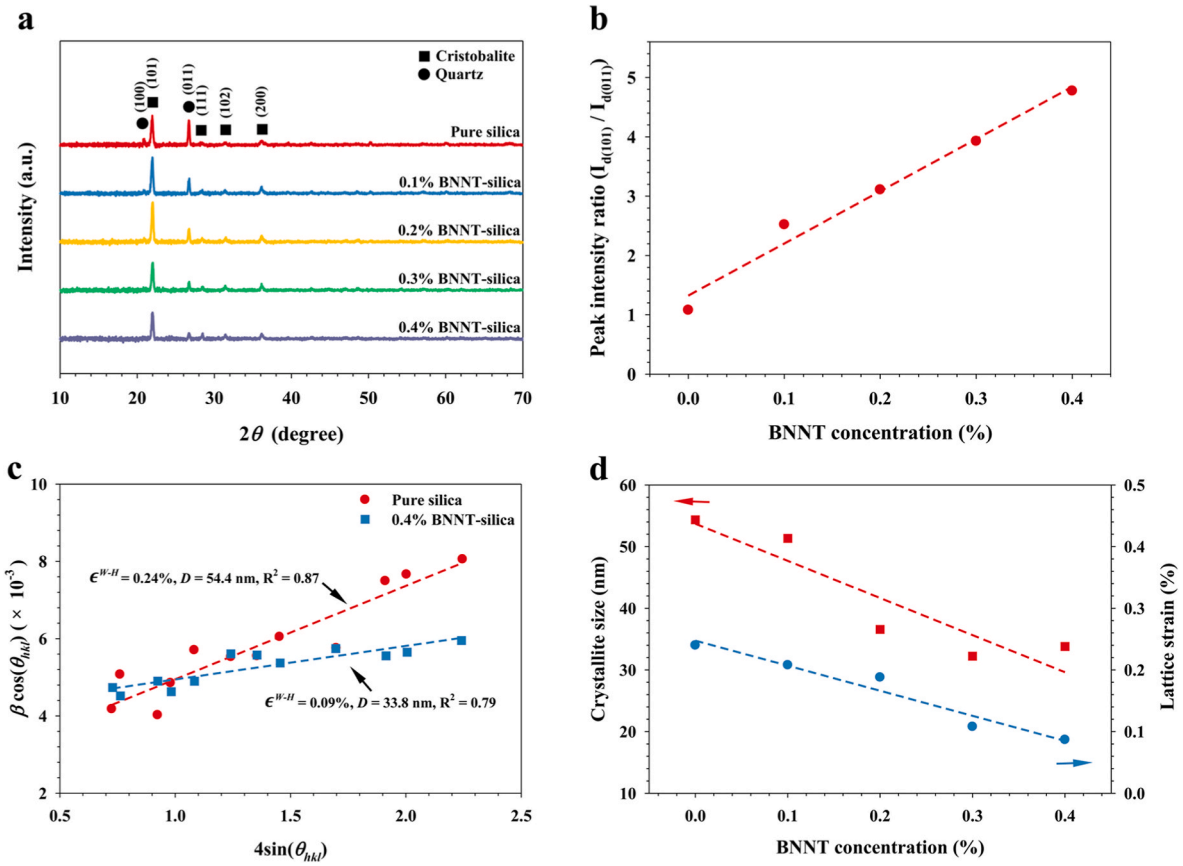

Fig. 10. Microstructural characterization of BNNT-silica nanocomposites: (a) XRD spectra of pure silica and BNNT-silica; (b) XRD peak intensity ratio of cristobalite (d101) to quartz (d011); (c) Representative Williamson-Hall plots of pure silica and 0.4 % BNNT-silica; (d) Crystalline size and lattice strain in BNNT-silica obtained using Williamson-Hall analysis approach.

content. A linear increase in this ratio with increasing BNNT concentration suggests that BNNTs promote the phase transformation from quartz to cristobalite during processing. The Williamson–Hall method is used to estimate the average crystallite size and lattice strain, based on the following relation [49]:

$$\beta \cos \theta_{hkl} = \frac{k\lambda}{D} + 4\epsilon^{W-H} \sin \theta_{hkl}, \quad (3)$$

where β denotes the full width at half maximum (FWHM) of the diffraction peak, θ_{hkl} is the diffraction angle, λ is the X-ray wavelength (1.54 Å for Cu Kα radiation), k is the shape factor ($k = 0.9$ for spherical particles), D is the crystallite size, and ϵ^{W-H} is the lattice strain. Using Equation 3, the crystallite size and lattice strain are calculated for pure silica and 0.4 % BNNT-silica, as shown in Fig. 10c. The results indicate that the incorporation of BNNTs leads to a significant reduction in lattice strain (from 0.24 % to 0.09 %) and crystallite size (from 54.4 nm to 33.8 nm). Fig. 10d shows that the crystallite size and lattice strain of the silica matrix decrease nearly linearly with increasing BNNT content. According to the Hall-Petch relationship, a reduced crystallite size corresponds to a higher density of grain boundaries, which hinders dislocation motion and thereby enhances strength and toughness [50]. The reduction in lattice strain enhances mechanical performance by mitigating internal stress concentrations and fostering a more uniform crystalline microstructure [51]. Overall, these results demonstrate that BNNTs induce favorable microstructural modifications in 3D-printed silica, thereby enhancing bulk mechanical properties. Such microstructural refinement represents one of the key reinforcing mechanisms in BNNT-ceramic nanocomposites, as illustrated in Fig. 3.

4. Conclusions

This study demonstrates the significant potential of BNNTs as effective reinforcements for enhancing the mechanical performance of 3D-printed ceramics. The addition of small amounts of BNNTs yields pronounced improvements in flexural strength and fracture toughness, driven by effective interfacial load transfer and BNNT-induced microstructural refinement within the silica matrix. Single-nanotube pullout experiments reveal exceptionally strong interfacial bonding, indicating that the reinforcing capability of BNNTs can be further amplified by addressing the inherent brittleness of ceramic matrices. These findings provide valuable insights into the reinforcement mechanisms at play in BNNT-ceramic systems, laying a foundation for the optimal design of lightweight, robust, and durable ceramics for structural applications.

CRediT authorship contribution statement

Dingli Wang: Writing – review & editing, Writing – original draft, Methodology, Investigation, Formal analysis. **Zihan Liu:** Writing – review & editing, Investigation, Formal analysis. **Nasim Anjum:** Writing – review & editing, Investigation, Formal analysis. **Yingchun Jiang:** Writing – review & editing, Investigation, Formal analysis. **Changhong Ke:** Writing – review & editing, Supervision, Methodology, Investigation, Funding acquisition, Formal analysis, Conceptualization.

Declaration of competing interest

The authors declare that they have no known competing financial interests or personal relationships that could have appeared to influence the work reported in this paper.

Acknowledgments

The authors gratefully acknowledge the support of the National Science Foundation under Grant Nos. CMMI 2009134, DMR 2406763, and CMMI 2425706, and the support of the SUNY System Administration through the SUNY Research Seed Grant Award #241008.

Appendix A. Supplementary data

Supplementary data to this article can be found online at https://doi.org/10.1016/j.ceramint.2025.11.251.

References

[1] J. Kim, J. Lee, J.-H. Ha, I.-H. Song, Effect of silica on flexibility of yttria-stabilized zirconia nanofibers for developing water purification membranes, Ceram. Int. 45 (2019) 17696–17704, https://doi.org/10.1016/j.ceramint.2019.05.337.

[2] X. Chen, W. Zheng, J. Zhang, C. Liu, J. Han, L. Zhang, C. Liu, Enhanced thermal properties of silica-based ceramic cores prepared by coating alumina/mullite on the surface of fused silica powders, Ceram. Int. 46 (2020) 11819–11827, https://doi.org/10.1016/j.ceramint.2020.01.216.

[3] D. Jia, L. Zhou, Z. Yang, X. Duan, Y. Zhou, Effect of preforming process and starting fused SiO_2 particle size on microstructure and mechanical properties of pressurelessly sintered BN_p/SiO_2 ceramic composites, J. Am. Ceram. Soc. 94 (2011) 3552–3560, https://doi.org/10.1111/j.1551-2916.2011.04540.x.

[4] J. Sun, D. Ye, J. Zou, X. Chen, Y. Wang, J. Yuan, H. Liang, H. Qu, J. Binner, J. Bai, A review on additive manufacturing of ceramic matrix composites, J. Mater. Sci. Technol. 138 (2023) 1–16, https://doi.org/10.1016/j.jmst.2022.06.039.

[5] Q. Li, X. Meng, X. Zhang, J. Liang, C. Zhang, J. Li, Y. Zhou, X. Sun, Enhanced 3D printed Al_2O_3 core via in-situ mullite, Addit. Manuf. 55 (2022) 102826, https://doi.org/10.1016/j.addma.2022.102826.

[6] F. Chen, Y.-R. Wu, J.-M. Wu, H. Zhu, S. Chen, S.-B. Hua, Z.-X. He, C.-Y. Liu, J. Xiao, Y.-S. Shi, Preparation and characterization of ZrO_2-Al_2O_3 bioceramics by stereolithography technology for dental restorations, Addit. Manuf. 44 (2021) 102055, https://doi.org/10.1016/j.addma.2021.102055.

[7] M. Li, H.-L. Huang, J.-M. Wu, Y.-R. Wu, Z.-A. Shi, J.-X. Zhang, Y.-S. Shi, Preparation and properties of Si_3N_4 ceramics via digital light processing using Si_3N_4 powder coated with Al_2O_3-Y_2O_3 sintering additives, Addit. Manuf. 53 (2022) 102713, https://doi.org/10.1016/j.addma.2022.102713.

[8] C.-J. Bae, D. Kim, J.W. Halloran, Mechanical and kinetic studies on the refractory fused silica of integrally cored ceramic mold fabricated by additive manufacturing, J. Eur. Ceram. Soc. 39 (2019) 618–623, https://doi.org/10.1016/j.jeurceramsoc.2018.09.013.

[9] H. Li, K. Hu, Y. Liu, Z. Lu, J. Liang, Improved mechanical properties of silica ceramic cores prepared by 3D printing and sintering processes, Scr. Mater. 194 (2021) 113665, https://doi.org/10.1016/j.scriptamat.2020.113665.

[10] Y.Y. Wang, L. Li, Z.Y. Wang, F.T. Liu, J.H. Zhao, P.P. Zhang, C. Lu, Fabrication of dense silica ceramics through a stereo lithography-based additive manufacturing, Solid State Phenom. 281 (2018) 456–462, https://doi.org/10.4028/www.scientific.net/SSP.281.456.

[11] M. Du, J.-Q. Bi, W.-L. Wang, X.-L. Sun, N.-N. Long, Microstructure and properties of SiO_2 matrix reinforced by BN nanotubes and nanoparticles, J. Alloys Compd. 509 (2011) 9996–10002, https://doi.org/10.1016/j.jallcom.2011.08.010.

[12] K. Zhang, Q. Meng, Z. Qu, R. He, A review of defects in vat photopolymerization additive-manufactured ceramics: characterization, control, and challenges, J. Eur. Ceram. Soc. 44 (2024) 1361–1384, https://doi.org/10.1016/j.jeurceramsoc.2023.10.067.

[13] Z. Liu, C. Ma, Z. Chang, P. Yan, F. Li, Advances in crack formation mechanism and inhibition strategy for ceramic additive manufacturing, J. Eur. Ceram. Soc. (2023), https://doi.org/10.1016/j.jeurceramsoc.2023.05.008. S0955221923003680.

[14] X. Wei, M.-S. Wang, Y. Bando, D. Golberg, Tensile tests on individual multi-walled boron nitride nanotubes, Adv. Mater. 22 (2010) 4895–4899, https://doi.org/10.1002/adma.201001829.

[15] Y. Jiang, N. Li, Z. Liu, C. Yi, H. Zhou, C. Park, C.C. Fay, J. Deng, H.B. Chew, C. Ke, Exceptionally strong boron nitride nanotube aluminum composite interfaces, Extreme Mech. Lett. 59 (2023) 101952, https://doi.org/10.1016/j.eml.2022.101952.

[16] N.G. Chopra, A. Zettl, Measurement of the elastic modulus of a multi-wall boron nitride nanotube, Solid State Commun. 105 (1998) 297–300.

[17] X. Chen, C.M. Dmuchowski, C. Park, C.C. Fay, C. Ke, Quantitative characterization of structural and mechanical properties of boron nitride nanotubes in high temperature environments, Sci. Rep. 7 (2017) 11388, https://doi.org/10.1038/s41598-017-11795-9.

[18] M.J. Tank, A.N. Reyes, J.G. Park, L.R. Scammell, M.W. Smith, A. De Leon, R. D. Sweat, Extreme thermal stability and dissociation mechanisms of purified boron nitride nanotubes: implications for high-temperature nanocomposites, ACS Appl. Nano Mater. 5 (2022) 12444–12453, https://doi.org/10.1021/acsanm.2c01965.

[19] M. Zheng, C. Ke, I.-T. Bae, C. Park, M.W. Smith, K. Jordan, Radial elasticity of multi-walled boron nitride nanotubes, Nanotechnology 23 (2012) 095703, https://doi.org/10.1088/0957-4484/23/9/095703.

[20] M. Zheng, X. Chen, I.-T. Bae, C. Ke, C. Park, M.W. Smith, K. Jordan, Radial mechanical properties of single-walled boron nitride nanotubes, Small 8 (2012) 116–121, https://doi.org/10.1002/smll.201100946.

[21] N. Li, C.M. Dmuchowski, Y. Jiang, C. Yi, F. Gou, J. Deng, C. Ke, H.B. Chew, Sliding energy landscape governs interfacial failure of nanotube-reinforced ceramic nanocomposites, Scr. Mater. 210 (2022) 114413, https://doi.org/10.1016/j.scriptamat.2021.114413.

[22] C. Yi, S. Bagchi, F. Gou, C.M. Dmuchowski, C. Park, C.C. Fay, H.B. Chew, C. Ke, Direct nanomechanical measurements of boron nitride Nanotube—ceramic interfaces, Nanotechnology 30 (2019) 025706, https://doi.org/10.1088/1361-6528/aae874.

[23] N. Anjum, D. Wang, F. Gou, C. Ke, Boron nitride nanotubes toughen silica ceramics 2 (2024) 735–746, https://doi.org/10.1021/acsaenm.4c00005.

[24] D. Wang, Z. Liu, R. Chen, A. Liu, N. Anjum, Y. Liu, F. Ning, C. Ke, Enhancing the strength and toughness of 3D-Printed alumina reinforced with boron nitride nanotubes, ACS Appl. Nano Mater. 8 (2025) 9481–9491, https://doi.org/10.1021/acsanm.5c01183.

[25] W.-L. Wang, J.-Q. Bi, K.-N. Sun, M. Du, N.-N. Long, Y.-J. Bai, Fabrication of alumina ceramic reinforced with boron nitride nanotubes with improved mechanical properties, J. Am. Ceram. Soc. 94 (2011) 3636–3640, https://doi.org/10.1111/j.1551-2916.2011.04821.x.

[26] N. Anjum, D. Wang, C. Ke, Toughening polymer-derived ceramics with boron nitride nanotubes, ACS Appl. Eng. Mater. (2025), https://doi.org/10.1021/acsaenm.5c00295.

[27] M. Tank, A.D. Leon, W. Huang, M. Patadia, J. Degraff, R. Sweat, Manufacturing of stereolithographic 3D printed boron nitride nanotube-reinforced ceramic composites with improved thermal and mechanical performance, Funct. Compos. Struct. 5 (2023) 015001, https://doi.org/10.1088/2631-6331/acb12a.

[28] M.W. Smith, K.C. Jordan, C. Park, J.-W. Kim, P.T. Lillehei, R. Crooks, J.S. Harrison, Very long single- and few-walled boron nitride nanotubes via the pressurized vapor/condenser method, Nanotechnology 20 (2009) 505604, https://doi.org/10.1088/0957-4484/20/50/505604.

[29] V. Yamakov, C. Park, J.H. Kang, X. Chen, C. Ke, C. Fay, Piezoelectric and elastic properties of multiwall boron-nitride nanotubes and their fibers: a molecular dynamics study, Comput. Mater. Sci. 135 (2017) 29–42, https://doi.org/10.1016/j.commatsci.2017.03.050.

[30] H. Ma, Q. Zhang, T. Meng, J. Yin, X. Fang, S. Yin, D. Yang, R. Zuo, Design and mechanical/thermal properties of in-situ synthesized mullite in SLA 3D printing Al_2O_3-SiO_2 ceramic, Ceram. Int. 51 (2025) 10726–10737, https://doi.org/10.1016/j.ceramint.2024.12.503.

[31] Y. Yu, B. Zou, X. Wang, C. Huang, Rheological behavior and curing deformation of paste containing 85 wt% Al_2O_3 ceramic during SLA-3D printing, Ceram. Int. 48 (2022) 24560–24570, https://doi.org/10.1016/j.ceramint.2022.05.099.

[32] E. Mitsoulis, Fountain flow of pseudoplastic and viscoplastic fluids, J. Non-Newtonian Fluid Mech. 165 (2010) 45–55, https://doi.org/10.1016/j.jnnfm.2009.09.001.

[33] G. Zhang, D. Carloni, Y. Wu, 3D printing of transparent YAG ceramics using copolymer-assisted slurry, Ceram. Int. 46 (2020) 17130–17134, https://doi.org/10.1016/j.ceramint.2020.03.247.

[34] Y. Wang, Z. Wang, S. Liu, Z. Qu, Z. Han, F. Liu, L. Li, Additive manufacturing of silica ceramics from aqueous acrylamide based suspension, Ceram. Int. 45 (2019) 21328–21332, https://doi.org/10.1016/j.ceramint.2019.07.118.

[35] T. Li, Y. Chen, W. Li, J. Li, L. Luo, T. Yang, L. Liu, G. Wu, Fabrication and mechanical properties of boron nitride nanotube reinforced silicon nitride ceramics, Ceram. Int. 44 (2018) 6456–6460, https://doi.org/10.1016/j.ceramint.2018.01.041.

[36] W. Wang, J. Bi, K. Sun, M. Du, N. Long, Y. Bai, Fabrication of alumina ceramic reinforced with boron nitride nanotubes with improved mechanical properties, J. Am. Ceram. Soc. 94 (2011) 3636–3640, https://doi.org/10.1111/j.1551-2916.2011.04821.x.

[37] W. Dong, C. Bao, K. Sun, H. Ma, S. Li, T. Liu, W. Lu, The fabrication of fiber-reinforced polyamine-coated silica paste and the mechanical properties of SiO_2/SiO_2 composites via stereolithography combined with silica sol impregnation, Addit. Manuf. 53 (2022) 102714, https://doi.org/10.1016/j.addma.2022.102714.

[38] B. Wang, A. Arab, J. Xie, P. Chen, The influence of microstructure on the flexural properties of 3D printed zirconia part via digital light processing technology, Materials 15 (2022) 1602, https://doi.org/10.3390/ma15041602.

[39] J. Fan, X. Xu, S. Niu, Y. Zhou, X. Li, Y. Guo, Y. Luo, Anisotropy management on microstructure and mechanical property in 3D printing of silica-based ceramic cores, J. Eur. Ceram. Soc. 42 (2022) 4388–4395, https://doi.org/10.1016/j.jeurceramsoc.2022.03.059.

[40] Z. Liu, K. Song, B. Gao, T. Tian, H. Yang, X. Lin, W. Huang, Microstructure and mechanical properties of Al_2O_3/ZrO_2 directionally solidified eutectic ceramic prepared by laser 3D printing, J. Mater. Sci. Technol. 32 (2016) 320–325, https://doi.org/10.1016/j.jmst.2015.11.017.

[41] P.K. Rao, P. Jana, M.I. Ahmad, P.K. Roy, Synthesis and characterization of zirconia toughened alumina ceramics prepared by co-precipitation method, Ceram. Int. 45 (2019) 16054–16061, https://doi.org/10.1016/j.ceramint.2019.05.121.

[42] Ch Androulidakis, E.N. Koukaras, M. Poss, K. Papagelis, C. Galiotis, S. Tawfick, Strained hexagonal boron nitride: phonon shift and grüneisen parameter, Phys. Rev. B 97 (2018) 241414, https://doi.org/10.1103/PhysRevB.97.241414.

[43] N. Anjum, O.Q. Alsmairat, Z. Liu, C. Park, C.C. Fay, C. Ke, Mechanical characterization of electrospun boron nitride nanotube-reinforced polymer nanocomposite microfibers, J. Mater. Res. 37 (2022) 4594–4604, https://doi.org/10.1557/s43578-022-00653-8.

[44] X. Ma, X. Kang, J. Cao, Origin of the elastic anisotropy of silica particles: insights from first-principles calculations and nanoindentation molecular dynamic simulations, Comput. Geotech. 159 (2023) 105489, https://doi.org/10.1016/j.compgeo.2023.105489.

[45] O.Q. Alsmairat, F. Gou, C.M. Dmuchowski, P.R. Chiarot, C. Park, R.N. Miles, C. Ke, Quantifying the interfacial load transfer in electrospun carbon nanotube polymer nanocomposite microfibers by using *in situ* Raman micromechanical characterization techniques, J. Phys. Appl. Phys. 53 (2020) 365302, https://doi.org/10.1088/1361-6463/ab8fdd.

[46] Y. Zhao, X. Chen, C. Park, C.C. Fay, S. Stupkiewicz, C. Ke, Mechanical deformations of boron nitride nanotubes in crossed junctions, J. Appl. Phys. 115 (2014) 164305, https://doi.org/10.1063/1.4872238.

[47] Y.-G. Miao, H.-Y. Liu, T. Suo, Y.-W. Mai, F.-Q. Xie, Y.-L. Li, Effects of strain rate on mechanical properties of nanosilica/epoxy, Composites, Part B 96 (2016) 119–124, https://doi.org/10.1016/j.compositesb.2016.04.008.

[48] R.F.S. Lenza, E.H.M. Nunes, D.C.L. Vasconcelos, W.L. Vasconcelos, Preparation of sol–gel silica samples modified with drying control chemical additives, J. Non-Cryst. Solids 423–424 (2015) 35–40, https://doi.org/10.1016/j.jnoncrysol.2015.05.010.

[49] M. Ghasemi Hajiabadi, M. Zamanian, D. Souri, Williamson-Hall analysis in evaluation of lattice strain and the density of lattice dislocation for nanometer scaled ZnSe and ZnSe:Cu particles, Ceram. Int. 45 (2019) 14084–14089, https://doi.org/10.1016/j.ceramint.2019.04.107.

[50] C.S. Pande, K.P. Cooper, Nanomechanics of hall–petch relationship in nanocrystalline materials, Prog. Mater. Sci. 54 (2009) 689–706, https://doi.org/10.1016/j.pmatsci.2009.03.008.

[51] Z. Li, M. Xiong, J. Lei, J. Li, Y. Chen, S. Zhang, Effect of Mo doping on the microstructures and mechanical properties of ZnO and AZO ceramics, Ceram. Int. 47 (2021) 30563–30571, https://doi.org/10.1016/j.ceramint.2021.07.234.